JBC RESEARCH ARTICLE

Temperature-dependent structural transition following X-ray-induced metal center reduction in oxidized cytochrome *c* oxidase

Received for publication, January 18, 2022, and in revised form, February 28, 2022 Published, Papers in Press, March 5, 2022,
https://doi.org/10.1016/j.jbc.2022.101799

Izumi Ishigami[1], **Silvia Russi**[2], **Aina Cohen**[2], **Syun-Ru Yeh**[1,*], **and Denis L. Rousseau**[1,*]

From the [1]*Department of Biochemistry, Albert Einstein College of Medicine, Bronx, New York, USA;* [2]*Structural Molecular Biology, Stanford Synchrotron Radiation Lightsource, SLAC National Accelerator Laboratory, Stanford University, Menlo Park, California, USA*

Edited by Ruma Banerjee

Cytochrome *c* oxidase (C*c*O) is the terminal enzyme in the electron transfer chain in the inner membrane of mitochondria. It contains four metal redox centers, two of which, Cu_B and heme a_3, form the binuclear center (BNC), where dioxygen is reduced to water. Crystal structures of C*c*O in various forms have been reported, from which ligand-binding states of the BNC and conformations of the protein matrix surrounding it have been deduced to elucidate the mechanism by which the oxygen reduction chemistry is coupled to proton translocation. However, metal centers in proteins can be susceptible to X-ray-induced radiation damage, raising questions about the reliability of conclusions drawn from these studies. Here, we used microspectroscopy-coupled X-ray crystallography to interrogate how the structural integrity of bovine C*c*O in the fully oxidized state (O) is modulated by synchrotron radiation. Spectroscopic data showed that, upon X-ray exposure, O was converted to a hybrid O* state where all the four metal centers were reduced, but the protein matrix was trapped in the genuine O conformation and the ligands in the BNC remained intact. Annealing the O* crystal above the glass transition temperature induced relaxation of the O* structure to a new R* structure, wherein the protein matrix converted to the fully reduced R conformation with the exception of helix X, which partly remained in the O conformation because of incomplete dissociation of the ligands from the BNC. We conclude from these data that reevaluation of reported C*c*O structures obtained with synchrotron light sources is merited.

Cytochrome *c* oxidase (C*c*O) is the terminal enzyme of the electron transport chain in the inner mitochondrial membrane in eukaryotes and the plasma membrane in prokaryotes (1–3). It catalyzes the four-electron reduction of dioxygen to two water molecules and harnesses the redox energy to pump four protons across the membrane against an electrochemical proton concentration gradient (2, 4).

$$O_2 + 4H^+ + 4e^- + 4H^+_{in} \rightarrow 2H_2O + 4H^+_{out}$$

* For correspondence: Denis L. Rousseau, denis.rousseau@einsteinmed.edu; Syun-Ru Yeh, syun-ru.yeh@einsteinmed.edu.

Crystal structures of bovine heart C*c*O (bC*c*O) show that it is a homodimer (5) with each monomer comprised of 13 subunits and four redox sites: Cu_A, heme *a*, Cu_B, and heme a_3 (Fig. 1*A*). Cu_B and heme a_3 constitute the so-called binuclear center (BNC), where dioxygen is reduced to water. During the reduction reaction, four electrons are sequentially passed from cytochrome *c via* Cu_A and heme *a* to the dioxygen bound to heme a_3 in the BNC; at the same time, four protons (the "substrate protons") are taken up from the negative side of the mitochondrial membrane to generate two water molecules. Coupled with the dioxygen reduction chemistry, four additional protons (the "pumped protons") are translocated from the negative to the positive side of the mitochondrial membrane (2).

Time-resolved studies showed that the oxygen reduction reaction follows a biphasic mechanism (Fig. 1*B*) (6–10). In the oxidative phase, the fully reduced enzyme (**R**) binds O_2 to form the O_2 complex (**A**), which then converts to the fully oxidized enzyme ($\mathbf{O_H}$) *via* the **P** and **F** intermediates, during which two electrons and two substrate protons (*blue*) are loaded into the BNC and two pumped protons (*green*) are translocated through the protein matrix to the positive side of the membrane. In the ensuing reductive phase, $\mathbf{O_H}$ converts back to the **R** state *via* the putative $\mathbf{E_H}$ intermediate, during which two additional electrons and two substrate protons (*blue*) are transferred into the BNC; at the same time, two water molecules are released, and two pump protons (*green*) are translocated. All the oxygen intermediates, except $\mathbf{E_H}$, have been identified spectroscopically (8–11).

The $\mathbf{O_H}$ intermediate produced at the end of the oxidative phase is redox equivalent to the resting oxidized **O** state, but if $\mathbf{O_H}$ is allowed to relax to **O**, its subsequent reduction to **R** is unable to drive proton translocation (6), indicating that $\mathbf{O_H}$ is structurally distinct from the resting **O** state. To identify the molecular origin enabling the $\mathbf{O_H}$ state, but not the **O** state, to translocate protons, it is important to fully understand the identity of the ligand(s) in the BNC and the conformations of the two heme groups, as well as the protein environment surrounding them in the two states. The crystal structures of bC*c*O, as well as several bacterial C*c*Os, in their resting **O** state have been reported (12–15). However, the identity of the ligand(s) in the BNC remains elusive. In bC*c*O (12), as well as in *Paracoccus denitrificans* C*c*O (14), the ligand was assigned as a

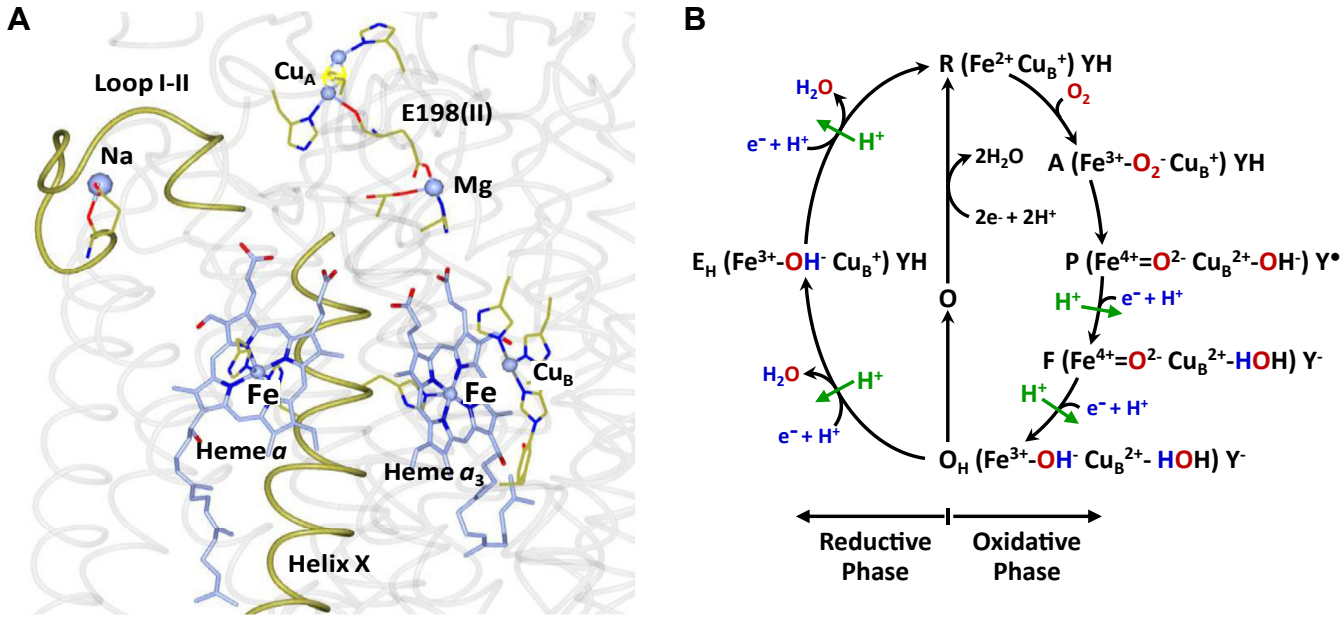

Figure 1. Structure of the metal centers in subunits I and II. In bC*c*O (*A*) and the proposed biphasic sequential mechanism (*B*). *A*, shows the locations of the four redox centers, Cu_A, heme *a*, Cu_B, and heme a_3, with respect to helix X and loop I–II in bC*c*O. The structure is from Protein Data Bank (ID: 7TIE). The Mg atom and the E198 from subunit II that links Mg to Cu_A are also shown as indicated. *B*, shows the proposed dioxygen reduction mechanism depicting the correlation of the changes in the oxidation and ligation states of the BNC with the entry of four electrons and four substrate protons (*in blue*) into the BNC and the translocation of four pumped protons (*in green*) (see the full description in the main text). If $\mathbf{O_H}$ produced at the end of the oxidative phase is allowed to relax to the resting **O** state, its reduction to **R** does not support proton translocation. bC*c*O, bovine heart C*c*O; BNC, binuclear center.

peroxide bridging the heme a_3 iron and Cu_B, but this assignment has been questioned (16, 17). Similar ambiguity exists in other bacterial C*c*Os, where the ligand density was modeled by a water coordinated to heme a_3 and a hydroxide ion coordinated to Cu_B (13) or a single hydroxide ion, or water, bridging the two metal centers (18, 19).

The characterization of the ligand identity in the BNC of C*c*O is complicated by X-ray-induced radiation damage (16, 20, 21). X-ray-induced radiation damage to protein crystals has been extensively studied (22, 23). An upper dose limit of 30,000 kGy for typical proteins has been established by Owen *et al.* (24). This dose limit is much lower for metalloproteins, ∼3 kGy, as metal centers in proteins are susceptible to photoinduced reduction and/or ligand dissociation (21, 25–28). Radiation-induced metal reduction in the oxidized forms of C*c*O crystals has been recognized based on optical spectra acquired following X-ray exposure (12, 18, 29–31), which raises an important question: do the structures solved by synchrotron light sources reflect the genuine forms of C*c*O? To address this question, here we sought to use microspectroscopy-coupled X-ray crystallography at the BL9-2 beamline at Stanford Synchrotron Radiation Lightsource (SSRL) to systematically interrogate the effects of synchrotron radiation on the structural properties of bC*c*O in the fully oxidized **O** state. As a comparison, a set of **O** and **R** structures were obtained at Sector 31 of the Advanced Photon Source (APS).

Results and discussion

X-ray-induced reduction of redox centers

We crystalized bC*c*O in the fully oxidized state, **O**, and acquired its diffraction data at 100 K with an X-ray exposure of ∼161 kGy at the BL9-2 beamline at SSRL. The structure was refined to a resolution of 2.35 Å (Protein Data Bank [PDB] ID: 7TIH, Table S1). It is similar to a higher resolution structure obtained at the APS (PDB ID: 7TIE, Table S1) and other reported structures of fully oxidized bC*c*O obtained with synchrotron light sources (32, 33). Prior to the diffraction measurement, an optical absorption spectrum of the crystal was acquired *in situ* with a microspectrometer equipped at the beamline. The spectrum has a Soret and visible band at 424 and ∼593 nm, respectively (Fig. 2*A*, spectrum a). It is in good agreement with that of the **O** state obtained in free solution (Fig. 2*B*, spectrum a, see the supporting information for the assignment of the bands). However, following the diffraction measurement, the crystal exhibited a new spectrum with (i) the appearance of a Soret band at 440 nm, at the expense of the 424 nm band (Fig. 2*A*, spectrum b), (ii) the development of a sharp visible band at ∼600 nm, and the concomitant reduction of the broad 593 nm band, and (iii) the growth of a small shoulder at ∼583 nm and two weak bands in the 500 to 560 nm region. We assign the spectral component with the 440 and 600 nm bands to a low-spin ferrous heme *a*, whereas the remaining component with the 424 and 593 nm bands to a low-spin ferrous heme a_3 with a sixth ligand coordinated to its iron (34, 35). The latter assignment is supported by the similarity of the visible bands to those of CO-bound reduced bC*c*O, where the ferrous heme a_3 is coordinated by the CO ligand (Fig. 2*B*, spectrum c). Associated with the changes in the heme-associated bands, the broad band at ∼900 nm, which is characteristic of the cupric Cu_A, disappeared (see the *upper inset* in Fig. 2*A*), indicating that Cu_A is reduced. Taken together, the spectral data suggest that all the four redox centers in bC*c*O are completely reduced by the X-ray beam, but the ligation state of the BNC is distinct from that in the

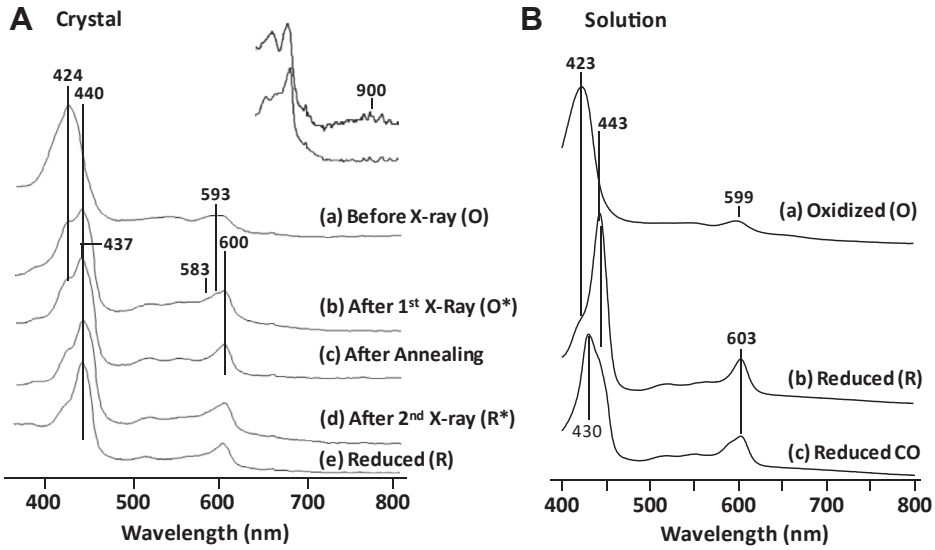

Figure 2. Absorption spectra of the fully oxidized bC*c*O crystal studied. In this work (*A*) *versus* those of bC*c*O obtained in free solution (*B*). *A*, spectra a and b were obtained before and after the first X-ray exposure, respectively; spectra c and d were obtained from the same crystal following annealing before and after the second X-ray exposure, respectively. Spectrum e is a reference spectrum of a fully reduced ligand-free crystal. The *upper right inset* displays an expanded view of spectrum a (*top*) and b (*bottom*) showing the presence of the broad band at ∼900 nm associated with Cu_A in the cupric state in spectrum a, which is absent in spectrum b. bC*c*O, bovine heart C*c*O.

fully reduced **R** state (spectrum b in Fig. 2), which is free of ligands. Structural comparison indicates that the protein structure is analogous to the authentic **O** structure obtained with serial femtosecond crystallography (PDB ID: 6NMP), where radiation damage is minimized (36), instead of the **R** structure (PDB ID: 7THU, Table S1), indicating that X-ray exposure during the diffraction measurement induces complete reduction of the four redox centers, but the protein matrix is locked in the fully oxidized **O** state. This hybrid state is referred to as **O*** hereinafter.

Annealing-induced protein conformational relaxation

We proposed that the **O*** state is stabilized at the cryogenic temperature because of limited protein motion. To allow the relaxation of the protein matrix, we annealed the **O*** crystal to above the protein glass transition temperature (∼200 K) for 2 s and then lowered the temperature back down to 100 K and acquired a new set of diffraction data at the same irradiated spot. In parallel, we obtained the *in-crystal* spectra before and after the diffraction measurement to identify potential changes in the redox and/or ligand coordination states of the metal centers.

As shown in spectrum c in Figure 2*A*, after annealing, the Soret band at 440 nm became somewhat sharper and shifted slightly to 437 nm, whereas the 424 nm band was slightly weakened. At the same time, the visible band at 600 nm was sharpened and the shoulders at 583 and 593 nm were diminished. These spectral features suggest the development of a new ligand-free ferrous heme a_3 component and small adjustment in the heme *a* conformation. Following the second diffraction measurement, only minor modifications in the spectrum were identified (spectrum d), which possibly reflect small fine-tuning in the protein matrix surrounding the redox centers. The data indicate that the second X-ray exposure did not lead to additional reduction of the redox centers, consistent with the view that the redox centers had been fully reduced by the first X-ray exposure. In general, the spectral data indicate that the annealing following the first X-ray exposure induced partial dissociation of the heme a_3 ligand as well as the relaxation of the heme *a* conformation and the protein matrix surrounding the redox centers. The fact that spectrum c and d are distinct from that of the fully reduced **R** species (spectrum e) indicates that the annealing treatment is insufficient to drive the full conversion of **O*** to **R**.

The structure of bC*c*O acquired following the annealing was solved to a resolution of 2.45 Å (PDB ID: 7TII, Table S1). This unique structure, referred to as **R*** hereinafter, is significantly different from the **O*** structure obtained prior to the annealing, in particular, in three structural regions, heme *a*, loop I–II, and helix X, where large differences were identified in the resting oxidized **O** *versus* the fully reduced **R** structures (Figs. S1 and S2). In the **R*** structure, the farnesyl side chain of heme *a* rotated by 120° with respect to that in the **O*** structure, such that the OH group forms a new H-bond with S34 instead of S382 (Fig. 3*A*, *green versus blue* structure), a hallmark of the reduced heme *a* (36). Likewise, loop I–II in the **R*** structure was best modeled with the conformation characteristic of the **R** structure, whereas that in the **O*** structure was best modeled with the conformation characteristic of the **O** structure (Fig. 3*B*, *green versus blue* structure). These data indicate that the annealing induces structural transitions in heme *a* and loop I–II from their oxidized conformations to their reduced conformations.

In contrast to heme *a* and loop I–II, the annealing-induced structural transition in the helix X region was more complicated. Helix X is a key structural element of bC*c*O, as it hosts the aforementioned S382 residue, as well as the proximal

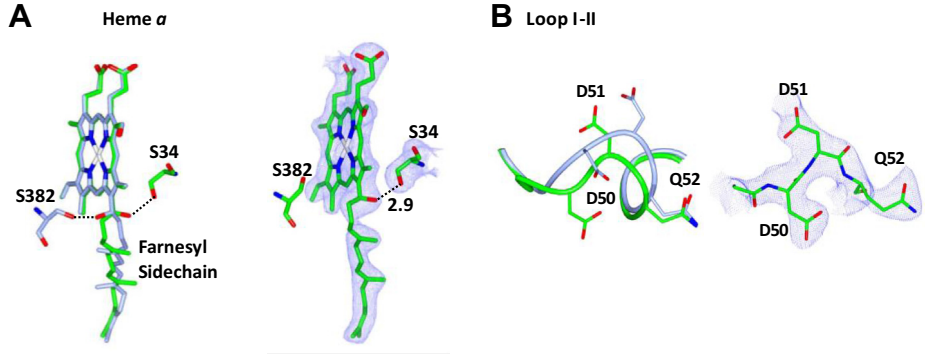

Figure 3. Electron density maps. Heme a (*A*) and loop I–II (*B*) in the **R*** state. The *left panels* of (*A*) and (*B*) show the structures of **R*** (***green***) overlaid with **O*** (***blue***) to highlight the annealing-induced structural transition. The $2F_O–F_C$ maps associated with the two structural elements in the **R*** state, shown in the *right panels*, are contoured at 1.25 σ and 1.5 σ, respectively. It is noted that there were no positive and negative features identifiable in the associated $F_O–F_C$ density maps countered at 3.0 σ (not shown).

ligands of heme *a* and heme a_3 (H378 and H376, respectively). Our previous studies showed that the conformation of helix X is sensitive to the ligand-binding state of heme a_3, regardless of its oxidation state (21) (Fig. S2). In the ligand-free ferrous state, it adopts a normal α-helical structure (referred to as the closed conformer [CC] hereinafter), but when a ligand binds to heme a_3, the helical structure of the [380–385] fragment is disrupted (21) (referred to as the open conformer [OC], hereinafter). The [380–385] fragment in the **O*** structure could be modeled with the OC without detectable features in the $F_O–F_C$ difference map, indicating the presence of a ligand coordinated to the ferrous heme a_3. In contrast, when the same fragment in the **R*** structure was modeled with the CC, unusually high *B*-factor values were detected in the 382-residue region (Fig. 4*B*, *trace b*); in addition, in the $F_O–F_C$ difference map, significant positive features coinciding with those expected for the OC were identified (Fig. 4*A*, panel *a*), suggesting the coexistence of the CC and OC. This scenario is in good agreement with the spectral data shown in Figure 2*A*, indicating partial dissociation of the heme a_3 ligand upon annealing. It is important to note that annealing-induced ligand dissociation following X-ray-induced reduction is not unprecedented. It has been documented in bacterial C*c*Os (18, 30) and in several ferric hemeprotein systems (27, 37), which share a common feature that the heme iron ligands (either a water or a hydroxide) are constrained in the heme

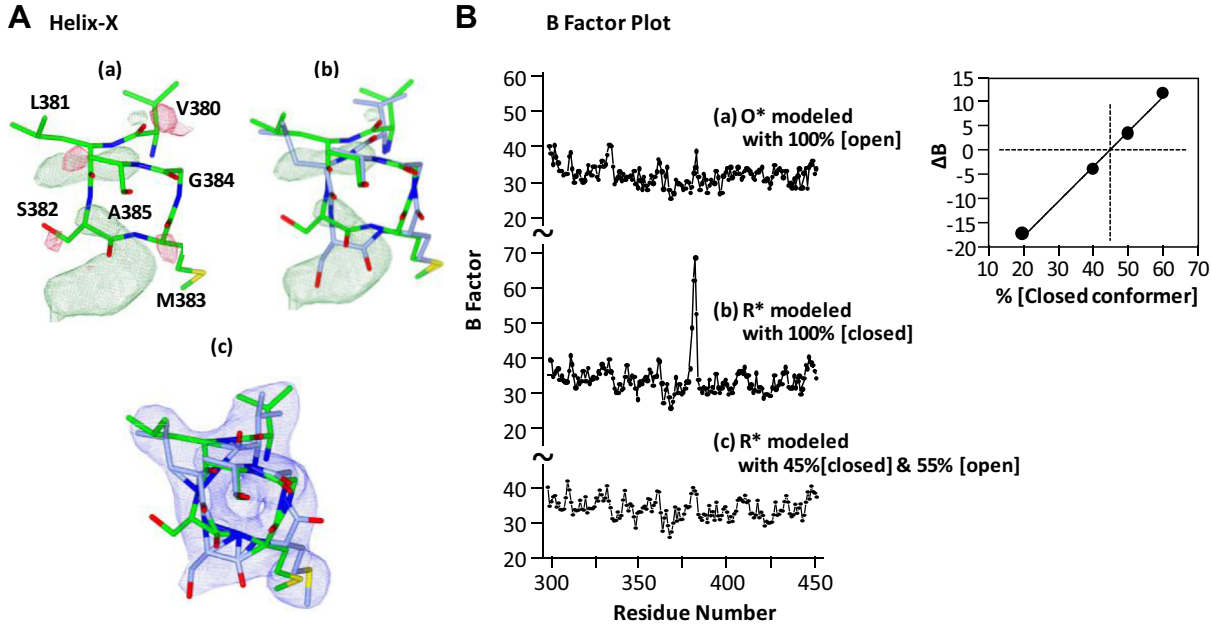

Figure 4. Electron density maps and *B*-factor plots of helix X in the R* state. *A*, the $F_O–F_C$ map obtained by modeling the **R*** structure with the closed conformer (*green sticks*) shown in (*A*) indicates that the electron density associated with helix X cannot be fully accounted by the pure closed conformer. The map is countered at 3.0 σ; the positive and negative features are shown in *green* and *red*, respectively. The residual positive features (*green*) were reproduced in (*B*) to demonstrate that they coincide well with the open conformer (*blue sticks*), indicating the coexist of the two conformers. The $2F_O–F_C$ map (countered at 1.25 σ) shown in (*C*) was obtained with the **R*** structure modeled with a mixed open conformer (55%) and closed conformer (45%); the absence of significant features in the $F_O–F_C$ map (contoured at 3.0 σ, not shown) supports the reliability of the modeling. *B*, the average backbone *B*-factors (in $Å^2$) of the **R*** structure obtained by modeling with the closed conformer (*B*) or with a mixed open (55%) and closed (45%) conformer (*C*). The comparable *B*-factor plot of the **O*** structure modeled with the open conformer is shown in (*A*) as a reference. The *right inset* shows a plot of ΔB as a function of the percent contribution of the closed conformer derived from the *B*-factor analysis described in the main text. The *crossed dashed lines* indicate that a mixed 55% open conformer and 45% closed conformer leads to ΔB = 0, where the averaged *B*-factors of the two conformers are comparable.

pockets when the metal centers were reduced and were unable to dissociate unless the temperature of the crystals was raised above the protein glass transition temperature.

To determine the relative contributions of the two conformers, we employed a *B*-factor analysis method (38). The **R*** structure was modeled with x[OC] + (1 – x)[CC], where the parameter "x" represents the fractional occupancy of the OC. We varied "x" and recorded ΔB, defined as the average backbone *B*-factor of the CC minus that of the OC in the [379–386] residue range. The average *B*-factors of the two conformers are predicted to be comparable; hence, ΔB is expected to be zero. Based on this analysis, we found that the **R*** structure was best modeled with a mixture of a 55% OC and a 45% CC (see the *right inset* in Fig. 4*B*). This structure assignment is supported by the observation that there are no detectable features in the F_O–F_C difference map when the **R*** structure was modeled with the mixed conformer (*structure c*, Fig. 4*A*), and that the *B*-factor plot of the final refined structure with the mixed conformer (*trace c*, Fig. 4*B*) is comparable with that of the **O*** structure (*trace a*).

Ligand-binding state of the BNC

To determine how the protein conformational relaxation correlates with the ligand-binding state of the BNC, we examined the electron density in the BNC of the **O*** and **R*** states. Strong ligand density was identified in the F_O–F_C difference map in the **O*** state when the ligand(s) were not modeled (Fig. 5*A*). In the **R*** state, the electron density was significantly reduced (Fig. 5*B*), but not entirely eliminated, consistent with the view that the ligand(s) are only partially dissociated from the BNC.

What is the identity of the ligand(s) in the BNC of the **O*** and **R*** states? As the **O*** and **R*** states are formed by X-ray exposure to the **O** state, [**O** → **O*** → **R***], it is important to first consider the structure of the **O** state. It has been proposed that the heme a_3 and Cu_B in the resting oxidized **O** state are bridged by a peroxide, with the [Fe^{3+}–O^-–O^-–Cu_B^{2+}] configuration (12, 39). However, it is unclear how the peroxide is formed in the BNC and what prevents the peroxide from spontaneous O–O bond scission. Moreover, modeling the ligand density with an unrestrained O–O bond leads to a structure with an excessively long O–O bond distance (1.75–1.9 Å) (12, 39). Here, we hypothesize that, in the resting **O** state, heme a_3 and Cu_B are coordinated by a hydroxide ion and a water molecule, respectively [Fe^{3+}–OH^-…H_2O–Cu_B^{2+}], as that originally proposed for the structure of $\mathbf{O_H}$ based on spectroscopic studies conducted in free solutions (9) and that proposed for a comparable **O** structure of a bacterial aa_3 type of *Cc*O (13). In addition, we assume that X-ray-induced metal reduction does not affect the nature of the ligands, whereas annealing allows partial dissociation of the ligands from the BNC. Accordingly, we modeled the ligand density in **O*** and **R*** with OH^- and H_2O coordinated to heme a_3 and Cu_B, respectively.

As shown in Figure 5*C*, the ligand density in the **O*** state can be nicely accounted for by a OH^- ion that is coordinated to heme a_3 and a H_2O molecule that is 2.35 Å away from Cu_B. Although with the current resolution, H_2O and OH^- are indistinguishable, the presence of two oxygen-containing ligands in the BNC is evident (see the polder map (40) on the *left panel*). With two other water molecules in the vicinity of the BNC as an internal standard (assuming both water molecules have full occupancy) (Fig. S3), the occupancy of the

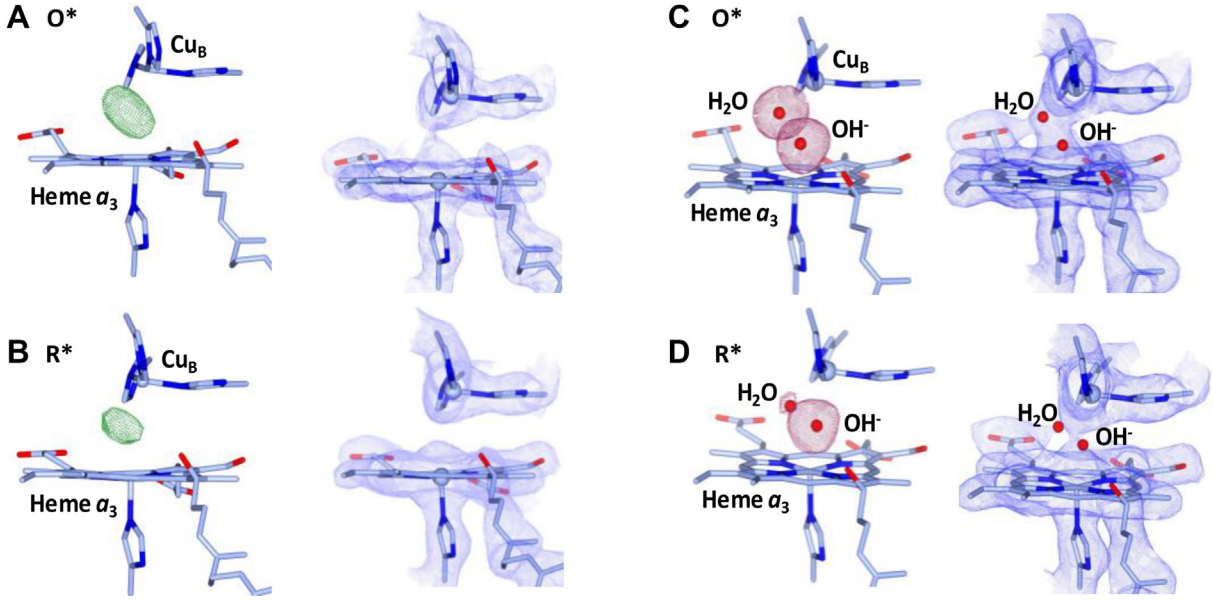

Figure 5. Ligand-binding state of the BNC in the O* *versus* R*. *A* and *B*, show the F_O–F_C maps (*left panels*) and $2F_O$–F_C maps (*right panels*), contoured at 7.00 and 1.50 σ, respectively, of the **O*** and **R*** states without the ligand modeled. The *green density* shown in the F_O–F_C maps highlight the unmodeled ligands in the BNC. *C* and *D*, show the polder maps of the ligands in the BNC of the **O*** and **R*** states, respectively (contoured at 4.5 σ), and the corresponding $2F_O$–F_C electron density maps with the ligands modeled with a hydroxide ion and a water molecule in the BNC (contoured at 1.00 σ). The ligand occupancies are estimated to be 86 and 80%, respectively, for **O*** and 63 and 35%, respectively, for **R***. No positive or negative features are identifiable in the associated F_O–F_C density maps contoured at 3.0 σ (not shown), supporting the reliability of the modeling. BNC, binuclear center.

OH^- and H_2O ligands was estimated to be 86 and 80%, respectively (Table S2). Similar results were obtained on a comparable oxidized enzyme (PDB ID: 7TIE, Fig. S4) obtained at the APS (although absorption spectra before and after X-ray exposure were not obtained). Likewise, the ligand density in the **R*** structure can be nicely accounted by OH^- and H_2O, with the occupancy of the OH^- ligand slightly reduced to 63%, whereas that of the H_2O ligand dramatically reduced to 35% (Fig. 5*D*, *left panel*). The $2F_O–F_C$ maps resulting from the modeling are shown in the *right panels* of Figure 5, *C* and *D*; the absence of detectable features in the corresponding $F_O–F_C$ difference maps supports the reliability of the fitting.

The O–O distance between the OH^- and the H_2O ligands in the **O*** structure is 1.95 Å, somewhat shorter than a typical H-bond. It is conceivable that the reduction of the metal centers in the BNC in the **O*** state leads to a high-energy configuration, $[Fe^{2+}–OH^-...H_2O–Cu_B{}^{1+}]$, where the two oxygen ligands are pushed together. It is notable that short O–O distances between the two oxygen ligands in the BNC of the oxidized forms of C*c*Os from *Thermus thermophilus* (TtC*c*O) have been reported. Specifically, crystallographic studies of caa_3 TtC*c*O carried out by Lyons *et al.* (41) showed that the ligand density was best modeled with a water molecule on heme a_3 and a hydroxide on Cu_B with an O–O separation of 2.3 Å. Similarly, density functional theory calculations of ba_3 TtC*c*O carried out by Du *et al.* (42) showed that when the ligands were modeled with a hydroxide coordinated to heme a_3 and a water coordinated to Cu_B, the O–O distance was 2.45 Å.

Conclusions

X-ray-induced reduction of metal centers can be problematic in structural determination of metalloproteins. Here, we demonstrated that X-ray exposure to the oxidized bC*c*O crystal during the diffraction measurements led to an **O*** structure, where the four redox centers were fully reduced, but its protein matrix was locked in the resting **O** structure at the cryogenic temperature employed. Although the reduction of the metal centers did not affect the polypeptide structure, the hydroxide and water ligands in the BNC were pushed together by the reduced heme a_3 iron and Cu_B. Annealing of the **O*** crystal to above the glass transition temperature enabled the relaxation of the protein to a new **R*** structure, where the polypeptide adopted the fully reduced **R** structure, except that the helix X partially remained in the **O** conformation as the ligands in the BNC were only partially dissociated. The incomplete transition of the **O*** structure to the fully reduced **R** structure upon annealing suggests a high-energy barrier for ligand dissociation from the BNC during the **O** → **R** transition in the oxygen reduction cycle.

Experimental procedures

Sample preparation

C*c*O was isolated and purified from bovine hearts by standard procedures (43, 44). The protein was further purified by concentrating it in an Amicon apparatus with a 200 kD molecular weight cutoff filter, where it was crystallized as microcrystals. The microcrystals were harvested and redissolved in pH 6.8 phosphate buffer (40 mM) containing 0.2% decylmaltoside to generate the crystallization protein stock. This as-prepared resting oxidized enzyme has a Soret absorption peak at 424 nm, characteristic of the "fast" enzyme (45, 46) (Fig. 2). The crystals were grown in pH 6.8 phosphate buffer (40 mM) with 0.2% decylmaltoside and 2.5% PEG4000, using an under-oil batch method. Nanocrystal seeds were included in the crystallization solution to ensure the reproducibly of the crystals. To produce the seeding solution, large crystals were crashed and sonicated in the mother solution. The large plate-like crystals, with a typical size of 400 × 400 × 80 μm, were harvested and cryoprotected by 45% ethylene glycol using a stepwise soaking protocol. The crystals were then flash frozen in liquid nitrogen.

Diffraction and optical absorption measurements

The before and after annealing diffraction data were obtained at a cryogenic temperature (100 K) at the beamline BL9-2 at the SSRL. The X-ray beam size was 100 × 60 μm, and the photon flux was 4.3×10^{10} (photons/s). We first acquired an absorption spectrum of the fully oxidized crystal to ensure its integrity. We then collected the first set of diffraction data to determine its structure. After the diffraction measurement, we acquired another absorption spectrum to examine X-ray-induced changes to the redox centers. We next blocked the cold nitrogen stream, which maintained the temperature of the crystal at 100 K, for 2 s until the temperature of the crystal was raised above the protein glass transition temperature (∼200 K), to promote the relaxation of the protein matrix. We then acquired a new set of diffraction data to determine the structural impact of the annealing. We acquired the absorption spectra of the crystal before and after the second diffraction measurement to examine the annealing-induced structural changes and the impact of the second X-ray exposure.

All the absorption spectra were obtained *in situ* with a microspectrometer equipped at the beamline BL9-2. The light beam, coinciding with the X-ray beam, was directed to the sample along the shortest axis of the plate-like crystal, to ensure that the whole spectrum in the 400 to 1000 nm region could be measured without saturation problems. The spot size of the light beam (∼50 × 50 μm) was much smaller than that of the X-ray beam (∼100 × 60 μm), which ensured that only the X-ray-irradiated area was probed.

The X-ray diffraction data of the resting oxidized **O** and fully reduced **R** crystals were acquired at the APS at the Argonne National Laboratory as references. The X-ray beam size was 110 × 80 μm, the photon flux was 3.6×10^{12} (photons/s). The fully reduced **R** crystal was prepared by soaking the **O** crystal with dithionite under anaerobic conditions. The complete reduction of the crystal was confirmed by optical absorption measurements.

Diffraction data analysis

The diffraction images were indexed, integrated, and scaled with XDS (47) and AIMLESS (48). Molecular replacement was

conducted with Phaser (49, 50) through the CCP4i graphic interface (51). Further model building was performed using COOT (52). Structure refinements were performed using Refmac5 (51, 53, 54). Data processing and refinement statistics are summarized in Table S1. The structural models were displayed with CCP4MG (55).

Data availability

The atomic parameters and structure factors (PDB IDs: 7TIH, 7TII, 7TIE, and 7THU) have been deposited in the PDB (https://www.rcsb.org/). All other data are contained within the article and can be shared upon request.

Supporting information—This article contains supporting information (21, 34, 45, 46).

Acknowledgments—Use of the Stanford Synchrotron Radiation Lightsource, SLAC National Accelerator Laboratory, is supported by the US Department of Energy (DOE), Office of Science, Office of Basic Energy Sciences under contract no. DE-AC02-76F00515. The SSRL Structural Molecular Biology Program is support by the DOE Office of Biological and Environmental Research and the National Institutes of Health, National Institute of General Medical Sciences (grant no.: P30GM133894). The reference structural data were collected by the Lilly Research Laboratories Collaborative Access Team beamline staff at Sector 31 of the Advanced Photon Source (APS). This research used resources of the APS, a US DOE Office of Science User Facility operated for the DOE Office of Science by Argonne National Laboratory under contract number DE-AC02-06CH11357. Use of the Lilly Research Laboratories Collaborative Access Team beamline at Sector 31 of the APS was provided by Eli Lilly Company, which operates the facility.

Author contributions—I. I., S.-R. Y., and D. L. R. conceptualization; I. I. validation; I. I., S.-R. Y., and D. L. R. formal analysis; I. I., S.-R. Y., and D. L. R. writing–review & editing; I. I., S. R., and A. C. funding acquisition.

Funding and additional information—This study was supported by the National Institutes of Health National Institute of General Medical Sciences grants R01 GM126297 (to D. L. R. and S.-R. Y.), R21 GM127944 (to D. L. R.), and R01 GM115773 (to S.-R. Y.). The content is solely the responsibility of the authors and does not necessarily represent the official views of the National Institute of General Medical Sciences or the National Institutes of Health.

Conflict of interest—The authors declare that they have no conflicts of interest with the contents of this article.

Abbreviations—The abbreviations used are: APS, Advanced Photon Source; BNC, binuclear center; bC*c*O, bovine heart C*c*O; CC, closed conformer; C*c*O, cytochrome *c* oxidase; DOE, Department of Energy; heme *a* and heme a_3, heme A moieties in bC*c*O; **O***, a hybrid derivative of resting oxidized bC*c*O resulting from X-ray-induced metal reduction; OC, open conformer; PDB, Protein Data Bank; **R***, a bC*c*O derivative produced by annealing the **O*** species; SSRL, Stanford Synchrotron Radiation Lightsource; TtC*c*O, C*c*Os from *Thermus thermophilus*.

References

1. Sousa, F. L., Alves, R. J., Ribeiro, M. A., Pereira-Leal, J. B., Teixeira, M., and Pereira, M. M. (2012) The superfamily of heme-copper oxygen reductases: Types and evolutionary considerations. *Biochim. Biophys. Acta* **1817**, 629–637
2. Belevich, I., and Verkhovsky, M. I. (2008) Molecular mechanism of proton translocation by cytochrome c oxidase. *Antioxid. Redox Signal.* **10**, 1–29
3. Wikstrom, M., and Sharma, V. (2018) Proton pumping by cytochrome c oxidase - a 40year anniversary. *Biochim. Biophys. Acta Bioenerg.* **1859**, 692–698
4. Yoshikawa, S., and Shimada, A. (2015) Reaction mechanism of cytochrome C oxidase. *Chem. Rev.* **115**, 1936–1989
5. Tsukihara, T., Aoyama, H., Yamashita, E., Tomizaki, T., Yamaguchi, H., Shinzawa-Itoh, K., Nakashima, R., Yaono, R., and Yoshikawa, S. (1996) The whole structure of the 13-subunit oxidized cytochrome c oxidase at 2.8 A. *Science* **272**, 1136–1144
6. Verkhovsky, M. I., Jasaitis, A., Verkhovskaya, M. L., Morgan, J. E., and Wikstrom, M. (1999) Proton translocation by cytochrome c oxidase. *Nature* **400**, 480–483
7. Rousseau, D. L. (1999) Bioenergetics. Two phases of proton translocation. *Nature* **400**, 412–413
8. Babcock, G. T., and Varotsis, C. (1993) Discrete steps in dioxygen activation–the cytochrome oxidase/O2 reaction. *J. Bioenerg. Biomembr.* **25**, 71–80
9. Han, S., Takahashi, S., and Rousseau, D. L. (2000) Time dependence of the catalytic intermediates in cytochrome c oxidase. *J. Biol. Chem.* **275**, 1910–1919
10. Kitagawa, T., and Ogura, T. (1998) Time-resolved resonance Raman investigation of oxygen reduction mechanism of bovine cytochrome c oxidase. *J. Bioenerg. Biomembr.* **30**, 71–79
11. Varotsis, C., Zhang, Y., Appelman, E. H., and Babcock, G. T. (1993) Resolution of the reaction sequence during the reduction of O2 by cytochrome oxidase. *Proc. Natl. Acad. Sci. U. S. A.* **90**, 237–241
12. Aoyama, H., Muramoto, K., Shinzawa-Itoh, K., Hirata, K., Yamashita, E., Tsukihara, T., Ogura, T., and Yoshikawa, S. (2009) A peroxide bridge between Fe and Cu ions in the O2 reduction site of fully oxidized cytochrome c oxidase could suppress the proton pump. *Proc. Natl. Acad. Sci. U. S. A.* **106**, 2165–2169
13. Qin, L., Hiser, C., Mulichak, A., Garavito, R. M., and Ferguson-Miller, S. (2006) Identification of conserved lipid/detergent-binding sites in a high-resolution structure of the membrane protein cytochrome c oxidase. *Proc. Natl. Acad. Sci. U. S. A.* **103**, 16117–16122
14. Koepke, J., Olkhova, E., Angerer, H., Muller, H., Peng, G., and Michel, H. (2009) High resolution crystal structure of Paracoccus denitrificans cytochrome c oxidase: New insights into the active site and the proton transfer pathways. *Biochim. Biophys. Acta* **1787**, 635–645
15. Tiefenbrunn, T., Liu, W., Chen, Y., Katritch, V., Stout, C. D., Fee, J. A., and Cherezov, V. (2011) High resolution structure of the ba3 cytochrome c oxidase from Thermus thermophilus in a lipidic environment. *PLoS One* **6**, e22348
16. Wikstrom, M. (2012) Active site intermediates in the reduction of O(2) by cytochrome oxidase, and their derivatives. *Biochim. Biophys. Acta* **1817**, 468–475
17. Kim, E., Chufan, E. E., Kamaraj, K., and Karlin, K. D. (2004) Synthetic models for heme-copper oxidases. *Chem. Rev.* **104**, 1077–1133
18. Liu, B., Chen, Y., Doukov, T., Soltis, S. M., Stout, C. D., and Fee, J. A. (2009) Combined microspectrophotometric and crystallographic examination of chemically reduced and X-ray radiation-reduced forms of cytochrome ba3 oxidase from thermus thermophilus: Structure of the reduced form of the enzyme. *Biochemistry* **48**, 820–826
19. Andersson, R., Safari, C., Dods, R., Nango, E., Tanaka, R., Yamashita, A., Nakane, T., Tono, K., Joti, Y., Bath, P., Dunevall, E., Bosman, R., Nureki, O., Iwata, S., Neutze, R., *et al.* (2017) Serial femtosecond crystallography structure of cytochrome c oxidase at room temperature. *Sci. Rep.* **7**, 4518
20. Kaila, V. R., Oksanen, E., Goldman, A., Bloch, D. A., Verkhovsky, M. I., Sundholm, D., and Wikstrom, M. (2011) A combined quantum chemical and crystallographic study on the oxidized binuclear center of cytochrome c oxidase. *Biochim. Biophys. Acta* **1807**, 769–778

21. Ishigami, I., Zatsepin, N. A., Hikita, M., Conrad, C. E., Nelson, G., Coe, J. D., Basu, S., Grant, T. D., Seaberg, M. H., Sierra, R. G., Hunter, M. S., Fromme, P., Fromme, R., Yeh, S.-R., and Rousseau, D. L. (2017) Crystal structure of CO-bound cytochrome c oxidase determined by serial femtosecond X-ray crystallography at room temperature. *Proc. Natl. Acad. Sci. U. S. A.* **114**, 8011–8016
22. Garman, E. F. (2010) Radiation damage in macromolecular crystallography: What is it and why should we care? *Acta Crystallogr. Section D, Biol. Crystallogr.* **66**, 339–351
23. Garman, E. F., and Owen, R. L. (2006) Cryocooling and radiation damage in macromolecular crystallography. *Acta Crystallogr. Section D, Biol. Crystallogr.* **62**, 32–47
24. Owen, R. L., Rudino-Pinera, E., and Garman, E. F. (2006) Experimental determination of the radiation dose limit for cryocooled protein crystals. *Proc. Natl. Acad. Sci. U. S. A.* **103**, 4912–4917
25. Beitlich, T., Kuhnel, K., Schulze-Briese, C., Shoeman, R. L., and Schlichting, I. (2007) Cryoradiolytic reduction of crystalline heme proteins: Analysis by UV-vis spectroscopy and X-ray crystallography. *J. Synchrotron Radiat.* **14**, 11–23
26. Yi, J., Orville, A. M., Skinner, J. M., Skinner, M. J., and Richter-Addo, G. B. (2010) Synchrotron X-ray-induced photoreduction of ferric myoglobin nitrite crystals gives the ferrous derivative with retention of the O-bonded nitrite ligand. *Biochemistry* **49**, 5969–5971
27. Denisov, I. G., Victoria, D. C., and Sligar, S. G. (2007) Cryoradiolytic reduction of heme proteins: Maximizing dose dependent yield. *Radiat. Phys. Chem.* **76**, 714–721
28. Pfanzagl, V., Beale, J. H., Michlits, H., Schmidt, D., Gabler, T., Obinger, C., Djinovic-Carugo, K., and Hofbauer, S. (2020) X-ray-induced photoreduction of heme metal centers rapidly induces active-site perturbations in a protein-independent manner. *J. Biol. Chem.* **295**, 13488–13501
29. Ueno, G., Shimada, A., Yamashita, E., Hasegawa, K., Kumasaka, T., Shinzawa-Itoh, K., Yoshikawa, S., Tsukihara, T., and Yamamoto, M. (2019) Low-dose X-ray structure analysis of cytochrome c oxidase utilizing high-energy X-rays. *J. Synchrotron Radiat.* **26**, 912–921
30. Liu, J., Qin, L., and Ferguson-Miller, S. (2011) Crystallographic and online spectral evidence for role of conformational change and conserved water in cytochrome oxidase proton pump. *Proc. Natl. Acad. Sci. U. S. A.* **108**, 1284–1289
31. Ferguson-Miller, S., Hiser, C., and Liu, J. (2012) Gating and regulation of the cytochrome c oxidase proton pump. *Biochim. Biophys. Acta* **1817**, 489–494
32. Yoshikawa, S., Shinzawa-Itoh, K., Nakashima, R., Yaono, R., Yamashita, E., Inoue, N., Yao, M., Fei, M. J., Libeu, C. P., Mizushima, T., Yamaguchi, H., Tomizaki, T., and Tsukihara, T. (1998) Redox-coupled crystal structural changes in bovine heart cytochrome c oxidase. *Science* **280**, 1723–1729
33. Yano, N., Muramoto, K., Shimada, A., Takemura, S., Baba, J., Fujisawa, H., Mochizuki, M., Shinzawa-Itoh, K., Yamashita, E., Tsukihara, T., and Yoshikawa, S. (2016) The Mg2+-containing water cluster of mammalian cytochrome c oxidase collects four pumping proton equivalents in each catalytic cycle. *J. Biol. Chem.* **291**, 23882–23894
34. Vanneste, W. H. (1966) The stoichiometry and absorption spectra of components a and a-3 in cytochrome c oxidase. *Biochemistry* **5**, 838–848
35. Argade, P. V., Ching, Y. C., and Rousseau, D. L. (1986) Resonance Raman spectral isolation of the a and a3 chromophores in cytochrome oxidase. *Biophysical J.* **50**, 613–620
36. Ishigami, I., Lewis-Ballester, A., Echelmeier, A., Brehm, G., Zatsepin, N., Grant, T., Jesse Coe, J., Lisova, S., Nelson, G., Zhang, S., Dobson, Z., Boutet, S., Sierra, R., Batyuk, A., Fromme, P., *et al.* (2019) Snapshot of an oxygen intermediate in the catalytic reaction of cytochrome c oxidase. *Proc. Nat. Acad. Sci. U. S. A.* **116**, 3572–3577
37. Engler, N., Ostermann, A., Gassmann, A., Lamb, D. C., Prusakov, V. E., Schott, J., Schweitzer-Stenner, R., and Parak, F. G. (2000) Protein dynamics in an intermediate state of myoglobin: Optical absorption, resonance Raman spectroscopy, and x-ray structure analysis. *Biophys. J.* **78**, 2081–2092
38. Shimada, A., Etoh, Y., Kitoh-Fujisawa, R., Sasaki, A., Shinzawa-Itoh, K., Hiromoto, T., Yamashita, E., Muramoto, K., Tsukihara, T., and Yoshikawa, S. (2020) X-ray structures of catalytic intermediates of cytochrome c oxidase provide insights into its O2 activation and unidirectional proton-pump mechanisms. *J. Biol. Chem.* **295**, 5818–5833
39. Hirata, K., Shinzawa-Itoh, K., Yano, N., Takemura, S., Kato, K., Hatanaka, M., Muramoto, K., Kawahara, T., Tsukihara, T., Yamashita, E., Tono, K., Ueno, G., Hikima, T., Murakami, H., Inubushi, Y., *et al.* (2014) Determination of damage-free crystal structure of an X-ray-sensitive protein using an XFEL. *Nat. Methods* **11**, 734–736
40. Liebschner, D., Afonine, P. V., Moriarty, N. W., Poon, B. K., Sobolev, O. V., Terwilliger, T. C., and Adams, P. D. (2017) Polder maps: Improving OMIT maps by excluding bulk solvent. *Acta Crystallogr. D Struct. Biol.* **73**, 148–157
41. Lyons, J. A., Aragao, D., Slattery, O., Pisliakov, A. V., Soulimane, T., and Caffrey, M. (2012) Structural insights into electron transfer in caa3-type cytochrome oxidase. *Nature* **487**, 514–518
42. Han Du, W. G., McRee, D., Gotz, A. W., and Noodleman, L. (2020) A water molecule residing in the Fea3(3+)...CuB(2+) Dinuclear center of the resting oxidized as-isolated cytochrome c oxidase: A density functional study. *Inorg. Chem.* **59**, 8906–8915
43. Yoshikawa, S., Choc, M. G., O'Toole, M. C., and Caughey, W. S. (1977) An infrared study of CO binding to heart cytochrome c oxidase and hemoglobin A. Implications re O2 reactions. *J. Biol. Chem.* **252**, 5498–5508
44. Mochizuki, M., Aoyama, H., Shinzawa-Itoh, K., Usui, T., Tsukihara, T., and Yoshikawa, S. (1999) Quantitative reevaluation of the redox active sites of crystalline bovine heart cytochrome c oxidase. *J. Biol. Chem.* **274**, 33403–33411
45. Baker, G. M., Noguchi, M., and Palmer, G. (1987) The reaction of cytochrome oxidase with cyanide. Preparation of the rapidly reacting form and its conversion to the slowly reacting form. *J. Biol. Chem.* **262**, 595–604
46. Moody, A. J., Cooper, C. E., and Rich, P. R. (1991) Characterisation of 'fast' and 'slow' forms of bovine heart cytochrome-c oxidase. *Biochim. Biophys. Acta* **1059**, 189–207
47. Otwinowski, Z., and Minor, W. (1997) Processing of X-ray diffraction data collected in oscillation mode. *Methods Enzymol.* **276**, 307–326
48. Evans, P. R., and Murshudov, G. N. (2013) How good are my data and what is the resolution? *Acta Crystallogr. D Biol. Crystallogr.* **D69**, 1204–1214
49. McCoy, A. J. (2007) Solving structures of protein complexes by molecular replacement with Phaser. *Acta Crystallographica. Section D, Biol. Crystallogr.* **63**, 32–41
50. McCoy, A. J., Grosse-Kunstleve, R. W., Adams, P. D., Winn, M. D., Storoni, L. C., and Read, R. J. (2007) Phaser crystallographic software. *J. Appl. Crystallogr.* **40**, 658–674
51. Winn, M. D., Ballard, C. C., Cowtan, K. D., Dodson, E. J., Emsley, P., Evans, P. R., Keegan, R. M., Krissinel, E. B., Leslie, A. G., McCoy, A., McNicholas, S. J., Murshudov, G. N., Pannu, N. S., Potterton, E. A., Powell, H. R., *et al.* (2011) Overview of the CCP4 suite and current developments. *Acta Crystallogr. Section D, Biol. Crystallogr.* **67**, 235–242
52. Emsley, P., and Cowtan, K. (2004) Coot: Model-building tools for molecular graphics. *Acta Crystallographica. Section D, Biol. Crystallogr.* **60**, 2126–2132
53. Murshudov, G. N., Skubak, P., Lebedev, A. A., Pannu, N. S., Steiner, R. A., Nicholls, R. A., Winn, M. D., Long, F., and Vagin, A. A. (2011) REFMAC5 for the refinement of macromolecular crystal structures. *Acta Crystallogr. Section D, Biol. Crystallogr.* **67**, 355–367
54. Murshudov, G. N., Vagin, A. A., and Dodson, E. J. (1997) Refinement of macromolecular structures by the maximum-likelihood method. *Acta Crystallogr. Section D, Biol. Crystallogr.* **53**, 240–255
55. McNicholas, S., Potterton, E., and Wilson, K. S. (2011) Presenting your structures: The CCP4mg molecular-graphics software. *Acta Crystallogr. D Biol. Crystallogr.* **D67**, 386–394